Distributed fiber optic strain sensing of bending deformation of a well mockup in the laboratory

Tsubasa Sasaki [a,*], Shenghan Zhang [b], Kenichi Soga [b], Linqing Luo [a], Barry Freifeld [a], Yoki Kitayama [c], Kyojiro Kawaguchi [c], Hitoshi Sugiyama [c]

[a] Earth Sciences Division, Lawrence Berkeley National Laboratory, 1 Cyclotron Road, Berkeley, CA, 94720, USA

[b] Department of Civil and Environmental Engineering, University of California–Berkeley, Berkeley, CA, 94720, USA

[c] Toyo Engineering Corporation, 2 Chome-8-1 Akanehama, Narashino, Chiba, 275-0024, Japan

[*] Corresponding author. E-mail address: tsubasasasaki@lbl.gov

Abstract

Well integrity is critical to the safety and success of subsurface energy exploration and management, as leakage of fluids from subsurface reservoirs is often induced by compromised wells. This study investigates bending deformation of a mockup of an oil/gas well that is subjected to loads expected in deviated wells under reservoir compaction and assesses the feasibility of utilizing distributed fiber optic strain sensing to monitor the deformation. A well mockup, which consists of outer and inner steel pipes with a cemented annulus, is tested under three-point bending loading and its strain and curvature development is monitored by Brillouin optical time domain reflectometry/analysis (BOTDR/A) as well as optical frequency domain reflectometry (OFDR). The primary objective of this research is to assess the strain sensing performance of newly fabricated fiber optic cables and to identify key cable characteristics which could improve the quality of distributed strain measurements with BOTDR/A. Results show that the tight-buffered cable is best suited for strain sensing as its maximum errors in the strain measurement were -36% and -24% against conventional sensors at the maximum elastic and plastic bending loads, respectively, whereas those of the non-tight-buffered cable were -45% and -71%, respectively. Similar trends were obtained in the bending curvature measurement. The detailed design of the tight-buffered cable is presented to elucidate key characteristics of such a cable, which will facilitate accurate distributed strain sensing in oil and gas wells.

Keywords
Distributed fiber optic sensing; distributed strain sensing; well integrity; well failure; fiber optic cable; real-time monitoring

1 Introduction

Well integrity is a critical factor in subsurface energy exploration and management, not only in a catastrophic event such as the Deepwater Horizon oil spill (McNutt, Camilli, et al. 2012; McNutt, Chu, et al. 2012; Hickman et al. 2012) but also in more subtle events such as gas leakage from CO_2 sequestration wells (Gasda, Bachu, and Celia 2004; Dou et al. 2020). In fact, many well integrity challenges occur in conventional oil and gas wells in compacting reservoirs, such as at the Wilmington field (Nagel 2001; Mayuga and Allen 1969; Roberts 1953), the Ekofisk field (Nagel 2001; Yudovich, Chin, and Morgan 1988; Schwall and Denney 1994), and the Belridge field (Dale, Narahara, and Stevens 1996; Fredrich et al. 2000). As such, well integrity is pertinent to global energy production and consumption; approximately 50% of the global energy in 2014 was still provided from oil and natural gas and their consumption had steadily been increasing from 1965 to 2014, especially in the highest energy consumer countries such as China, USA, and Russia (Aydin 2014; 2015; Aydin, Jang, and Topal 2016).

Fields with greater reservoir compaction exhibit more issues associated with loss of well integrity. Methane hydrate reservoirs, in particular, are at significant risk of compaction, as the reservoir layer usually consists of unconsolidated, soft sediment and substantial depressurization of pore water is carried out to produce methane gas from the reservoir (Yamamoto 2015; Yamamoto et al. 2014; Yoneda et al. 2015). Currently, a number of field tests have been carried out to examine the potential of methane hydrate reservoirs to produce an economic volume of methane gas to warrant commercial production (Chen et al. 2018; Klar et al. 2019; Yamamoto et al. 2017; Yamamoto 2015; Yamamoto and Dallimore 2008; Yamamoto et al. 2014). To ensure the long-term safety and viability of gas production, it is imperative to carry out real-time monitoring of well integrity in order to prevent unexpected well failures. This will contribute to improving not only the safety but also the environmental and management aspects of natural gas production, which are within the scope of natural gas science and engineering.

Distributed strain sensing (DSS) by fiber optics is an innovative approach to address the need of well integrity monitoring, as it is capable of measuring deformations of wells with high accuracy in real-time, which cannot be achieved by traditional distributed acoustic sensing (DAS) or temperature sensing (DTS) techniques. It has already been shown in a previous study (Sasaki et al. 2019) that Brillouin time domain reflectometry/analysis (BOTDR/A) is effective in monitoring the axial tensile deformation of a well mockup.

DSS by fiber optics has been implemented in boreholes for various purposes, including but not limited to subsurface subsidence monitoring (Zhang et al. 2018), hydromechanical characterization of the reservoir (Lei, Xue, and Hashimoto 2019; Sun et al. 2020; Y. Zhang et al. 2020; Sun et al. 2021), estimation of the flow of CO_2 plume in geological carbon storage (Sun et al. 2018), hydraulic fracturing monitoring (Krietsch et al. 2018), and monitoring of landslides (Kogure and Okuda 2018). Novel fiber optic cables have been developed which utilize chemo-mechanical coupling to detect hydrocarbon leakage in the well annulus (Wu 2019). Also, strain profiles in a fiber optic cable, which was embedded in a backfilled borehole, are shown to match those in the surrounding formation (i.e., no cable slippage at cable-formation interface) at moderate confining pressure levels, guaranteeing the quality of DSS data (Zhang et al. 2018). However, fiber optic cables deployed in oil and gas wells are usually not in direct contact with the formation, as the cables are typically cemented in the annulus behind the long casing string, which casts doubt upon the applicability of their DSS results to deep subsurface wells. Also, the cables employed in the above studies are not robust enough for in situ integrity monitoring of deep subsurface wells in actual oil and gas fields. The pressures and temperatures encountered require the cable to be engineered to resist the high collapse pressure and survive the elevated temperatures, while simultaneously maintaining the sensitivity to the deformation of the formation.

In the previous study (Sasaki et al. 2019), various fiber optic cables were tested in an axially deformed well mockup and evaluated for their robustness and strain sensitivity. It was found that the relevant factors for increasing strain sensitivity, while maintaining the robustness for surviving in downhole conditions, are tight-buffered coating layers around the optical fiber core and the number of coating layers (i.e., the greater the tight-buffer is and the less the number of coating layers is, the better the strain sensitivity).

A key challenge toward successful deployment of BOTDR/A in the field is the development of effective DSS cables. Commercially available fiber optic cables for DAS and DTS are not suitable for DSS as optical fibers in such cables are not tightly buffered to the outer cable sheath, which causes slippage of fibers and undermines the accuracy of distributed strain measurements. In this study, new fiber optic cables for DSS with BOTDR/A were developed and tested in a laboratory experiment. The fiber optic cables were embedded in the annulus of a laboratory-scale well mockup, which consisted of outer and inner steel pipes. The well mockup was then subjected to three-point bending to simulate bending deformation of a deviated well during reservoir compaction. A schematic diagram depicting the bending deformation of a deviated well during hypothetical compaction of a methane hydrate reservoir is provided in Figure 1.

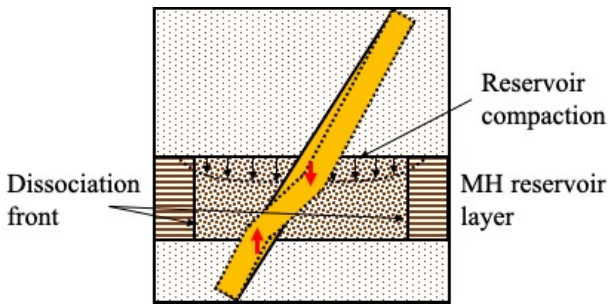

Figure 1 Bending well deformation in a methane hydrate reservoir [after Sasaki (2019)].

The primary objectives of this research are (i) to investigate the effectiveness of BOTDR/A to monitor bending deformation of the well mockup, (ii) to assess the performance of different fiber optic cables in monitoring strain and bending curvature development of the well mockup, and (iii) to identify key factors in oil and gas cables affecting the accuracy of BOTDR/A measurements. The following sections of the paper present details of the fiber optic cables and DSS techniques employed in this study, as well as details of mockup preparation, load testing, and test results.

2 Methodology

2.1 Distributed fiber optic strain sensing interrogators

Two distributed fiber optic strain sensing interrogators were employed to obtain the strain profiles of the well mockup; they are Omnisens Vision Dual interrogator and LUNA ODiSI 6104 interrogator (Figure

2). Both interrogators utilize backscattering of incident light waves traveling in an optical fiber to infer strain as well as temperature changes. The Omnisens measures the Brillouin backscattering spectra, which is generated due to the interaction of incident light waves and carrier-deformation waves, via a mechanism called Brillouin optical time domain reflectometry/analysis (BOTDR/A). The LUNA measures the Rayleigh backscattering spectra, which is caused by random refractive index fluctuations in an optical fiber, in the frequency domain via a mechanism called optical frequency domain reflectometry (OFDR). The LUNA interrogator is analogous to Fiber Bragg Grating (FBG) interrogators in the sense that OFDR utilizes an optical fiber as a long continuous array of weak FBGs with random periods.

(a) (b)

Figure 2 Distributed fiber optic strain sensing interrogators: (a) Omnisens Vision Dual BOTDR/A; (b) LUNA ODiSI 6104.

The shifts in the Brillouin/Rayleigh backscattering spectra and strain/temperature changes are correlated as shown in the following equations:

$$\Delta\nu_B = C_{\epsilon,B}\, \Delta\epsilon + C_{T,B}\, \Delta T \quad (1)$$

$$\Delta\nu_R = C_{\epsilon,R}\, \Delta\epsilon + C_{T,R}\, \Delta T \quad (2)$$

where $\Delta\nu_B$ is a frequency shift in the Brillouin backscattering spectra, $\Delta\nu_R$ is a frequency shift in the Rayleigh backscattering spectra, $C_{\epsilon,B}$ is the strain coefficient for Brillouin backscattering, $C_{T,B}$ is the temperature coefficient for Brillouin backscattering, $C_{\epsilon,R}$ is the strain coefficient for Rayleigh backscattering, $C_{T,R}$ is the temperature coefficient for Rayleigh backscattering, $\Delta\epsilon$ is a strain change, and ΔT is a temperature change. The values of the strain/temperature coefficients vary with interrogator and cable types. The coefficient values specific to the experimental settings of this study are provided in Table 1. Details about the cable types are provided in the following section.

Table 1 Strain and temperature coefficient values of the fiber optic cables.

Cable type	Interrogator type	Strain coefficient (MHz/%)	Temperature coefficient (MHz/˚C)
Cable 1 (ver. 1)	Omnisens	300	1.0
Cable 1 (ver. 2)	Omnisens	500	1.0
Cable 2	Omnisens	500	1.0
Cable 3	LUNA	$1.50 \cdot 10^6$	$1.57 \cdot 10^3$

The LUNA interrogator is capable of measuring precise strain profiles with extremely dense datapoints and high spatial resolution, to the point where submillimeter crack detection is possible (Zhang, Liu, Coulibaly, et al. 2020; Zhang, Liu, Cheng, et al. 2020). It is for this reason that the LUNA interrogator is used as the reference strain measurement in this study. A disadvantage of the LUNA interrogator is the short measurement length of up to 50 m, which makes it unsuitable for field measurements. BOTDR/A, on the other hand, measures averaged strain profiles over its spatial resolution of roughly 1 m but can measure tens of kilometers of strain/temperature profiles along a single fiber optic cable. Therefore, BOTDR/A is well suited to monitoring the mechanical/thermal behavior of infrastructure such as tunnels (Gue et al. 2015; Mohamad et al. 2012; 2010), bridges (Butler et al. 2016), pipelines (Inaudi and Glisic 2006), piles (Klar et al. 2006; Pelecanos et al. 2017; 2018; Mohamad et al. 2011), and subsurface wells (Sun et al. 2020; 2021). Further details for civil infrastructure applications can be found in Kechavarzi et al. (2016) and Soga and Luo (2018). Measurement performance characteristics of each interrogator are provided in Table 2.

Table 2 Measurement performance of the fiber optic interrogators.

	Omnisens Vision Dual (BOTDA)	LUNA ODiSI 6104
Spatial resolution (cm)	75	-- **
Sampling interval (cm)	25	0.26 *
Precision (2σ) (με)	±4	±6
Measurement distance (km)	60	0.050
Measurement rate (Hz)	N/A	10

* Sampling interval can range between 0.065 cm to 0.26 cm.

** The gauge length (i.e., spatial resolution) is undefined but increases with increasing sampling interval.

2.2 Fiber optic cables for DSS measurement

Three different fiber optic cables were examined in this study: Cable 1 (tight-buffered FIMT), Cable 2 (loose FIMT), and Cable 3 (non-FIMT baseline). The cross-sections of these cables are provided in Figure 3. The cross-section of the previous version of Cable 1, which was tested in a separate experiment prior to the present experiment, is also provided in Figure 3, which is referred to as Cable 1 (version 1). The primary difference between Cable 1 (ver. 1) and Cable 1 (ver. 2) is the axial separation between the fiber-optic elements; Cable 1 (ver. 2) has a reduced axial separation than Cable 1 (ver. 1) so as to improve strain transfer from the outer metal tube to the optical fibers. Details about the previous experiment are omitted as they significantly overlap with those of the present experiment.

Cable 1 is tailored for integrated monitoring of oil and gas wells. It is equipped with a DSS FIMT (fiber in metal tube) and a FIMT containing a DTS (distributed temperature sensing) fiber in a 1/4 in. OD metal tube. The outer metal tube is filled with polymer. The advantages of the current version of Cable 1 relative to the previous version are that (i) the DSS FIMT is tightly buffered to the metal sheath with an extra skim-coat polymer layer, (ii) the surface of the DTS FIMT is coated with a slip agent which enhances slippage and hence the strain-independence of the DTS FIMT, and (iii) the DSS FIMT is positioned closer to the center inside the cross-section of the metal sheath so as to improve strain transfer from the metal sheath to the DSS FIMT.

Cable 2 has been designed for integrated fiber-optic monitoring of oil and gas wells. The FIMT contains fibers for DAS (distributed acoustic sensing) and DTS. External to the FIMT is a tight buffered single-mode optical fiber (without a metal tube) for DSS.

Cable 3 was used with the LUNA interrogator for the reference strain measurement. It is a commercially available fiber optic cable that is often used in civil infrastructure monitoring (Cola et al. 2019; Rabaiotti et al. 2017; Fabris et al. 2021; Zhang, Liu, Coulibaly, et al. 2020). Its design is much simpler than that of

Cable 1 and 2 as it is not designed to survive in harsh subsurface conditions where oil and gas wells are usually constructed.

Distributed strain profiles along Cable 1 and 2 were measured with the Omnisens BOTDR/A interrogator, whereas those along Cable 3 were measured with the LUNA interrogator.

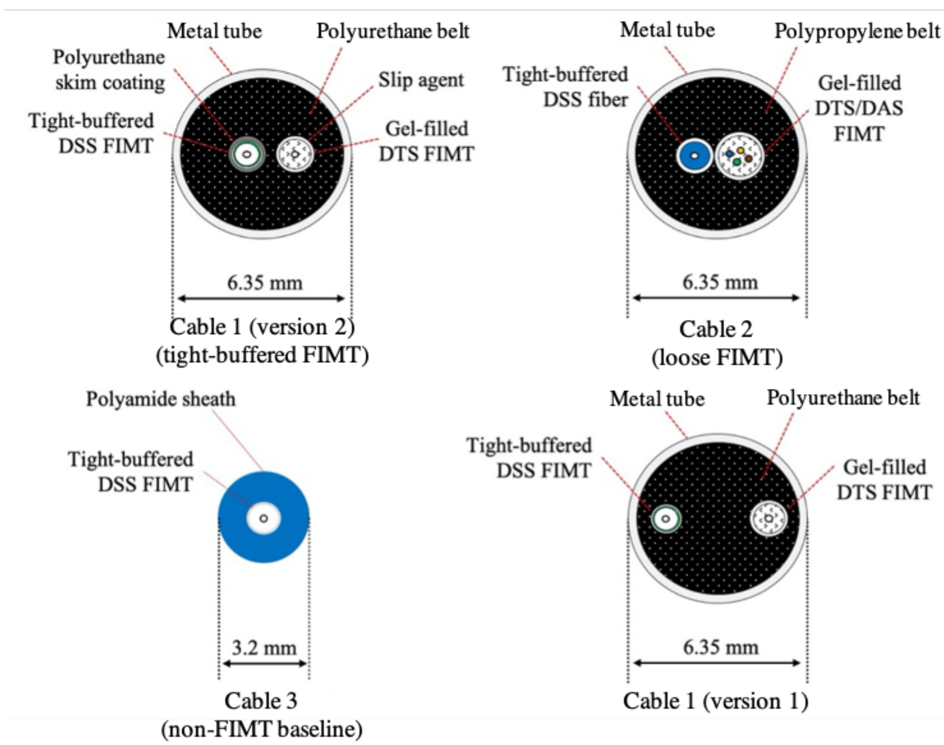

Figure 3 The cross-sections of the fiber optic cables examined in this research. Cable 1 (version 2), 2, and 3 are tested in the present experiment, whereas Cable 1 (version 1) was tested in a previous experiment.

3 Well mockup preparation

3.1 Configuration

Figure 4 shows the cross-sections of the well mockup. It consists of a 9 5/8 in. (0.24 m) OD (outer diameter) inner pipe and a 12 1/4 in. (0.31 m) ID (inner diameter) outer pipe with a wall thickness of 3/8 in. (9.53 mm) and 1/4 in. (6.35 mm), respectively. The inner pipe is assumed to be the casing and the deformation of the outer pipe mimics the strain transferred from the formation into the cement sheath., as the diameters of the pipes correspond to the diameter of casing and borehole of monitoring wells at the Nankai Trough (Yamamoto et al. 2014). The length of the mockup is 123 in. (3.12 m), which is roughly four times the spatial resolution of the Omnisens interrogator using the BOTDA mode. The support stand at the bottom of the concentric assembly is a spacer which creates a gap between the ground and the assembly. When it is positioned vertically to facilitate cementing, the gap protects the fiber optic cables from mechanical damage. As such, the support stand does not take any bending moment or shear stress and it has no effect on the bending behavior of the mockup.

At the beginning of mockup preparation, the pipes were separated as shown in Figure 5a. The inner pipe was inserted into the outer pipe after the fiber optic cables had been installed in the annulus to assemble the well mockup. There are eight cable sections in the mockup annulus as shown in Section A-A (Figure 4), which are created by aligning the holes on the top, bottom, and middle (gusset) plates (Figure 5b). These aligned holes ensured that the fiber optic cables were positioned parallel to the axis of the mockup and separated by a 45^{o} angle from one another in the circumferential direction.

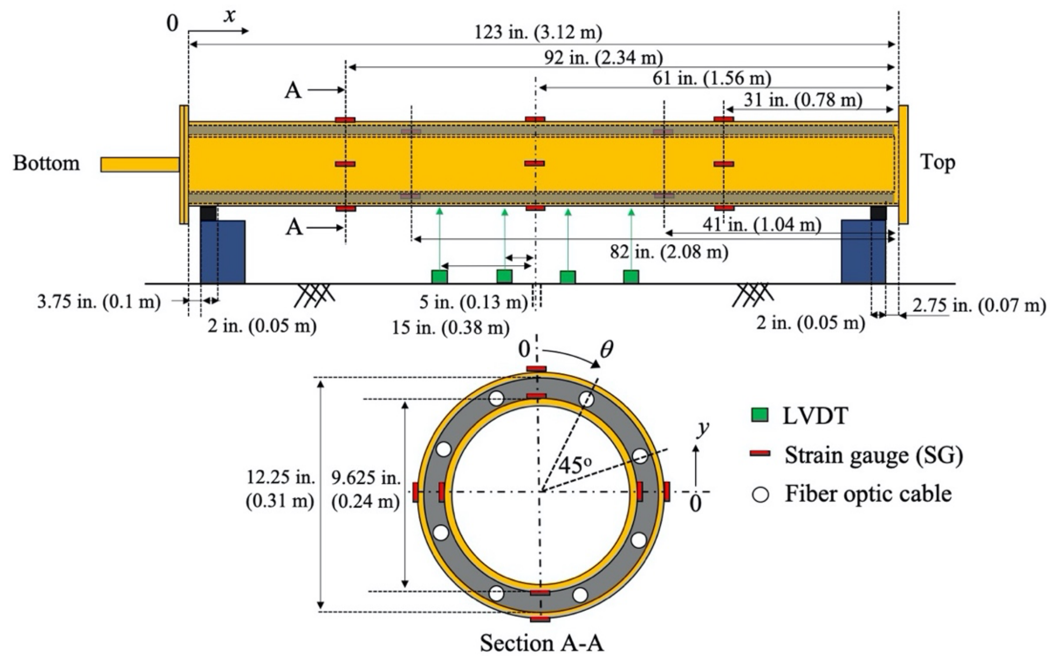

Figure 4 A cross-sectional schematic of the well mockup.

(a) (b)

Figure 5 The well mockup before assembling: (a) inner and outer pipes; (b) gusset plates at the middle length of the inner pipe that are attached for fiber optic cable installation.

3.2 Sensor installation

The well mockup was instrumented with strain gauges and LVDTs (linear variable differential transformers) to compare to fiber optic measurements. The locations of the sensors are shown in Figure 4. The strain gauges were attached on the surface of the inner and outer pipes at four circumferential locations, which were offset 90^{o} from one another, and at two (inner pipe) and three (outer pipe) longitudinal locations, respectively. The LVDTs were installed on the lower surface of the outer pipe at four longitudinal locations.

Figure 6 shows the locations of the fiber optic cables in the annulus of the well mockup. The fiber optic cables were installed prior to mockup assembling by passing through the cables along each annular segment (#1-#8). The cables were run through three longitudinally aligned holes in each segment (one hole each on the top, bottom, and middle gusset plates). In order to measure bending deformation, the cables of the same type were positioned diagonally across the circumferential cross-section of the mockup. For instance, Cable 1 was installed in the segment 1 and 5, Cable 2 in the segment 3 and 7, and Cable 3 in the segment 2, 4, 6, 8.

Cable 1 and 2 were spliced at the bottom exit of segment 3, 5 and 7 to form a closed loop which is a prerequisite for performing Omnisens measurements in the BOTDA mode. Cable 3 was terminated at the bottom exit of segment 8 to eliminate back reflection of the input light so as to increase the precision of LUNA measurements.

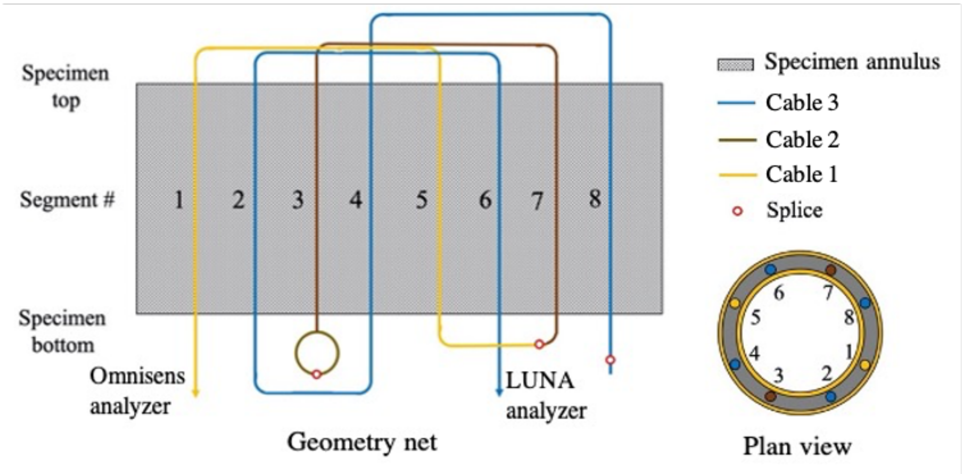

Figure 6 The positions of the fiber optic cables in the mockup annulus.

3.3 Annulus cementing

After the fiber optic cable installation, the mockup was set up vertically and fixed against a steel column so that cementing could be carried out. Cement slurry was prepared by mixing Portland cement with water at a 0.44 water-to-cement ratio. A 0.75% by volume shrinkage reducing admixture was added to the slurry while it was mixed. Slurry was mixed in four separate batches by a handheld drill at a rotation speed of about 1,000 rpm (rotation per minute) for 10 min before each batch was poured into the mockup annulus. The cement was cured under room temperature and humidity conditions for five days prior to the bending test.

4 Bending loading experiment

4.1 Loading scheme

After five days of cement cure, the mockup was set up in the loading frame (Figure 7). Bending loading was applied by pulling the fixture attached at the middle of the mockup downward. This was accomplished by connecting the fixture with a rod that passes through a hole in the floor down to the basement ceiling where the rod couples to an actuator and a load cell.

(a)

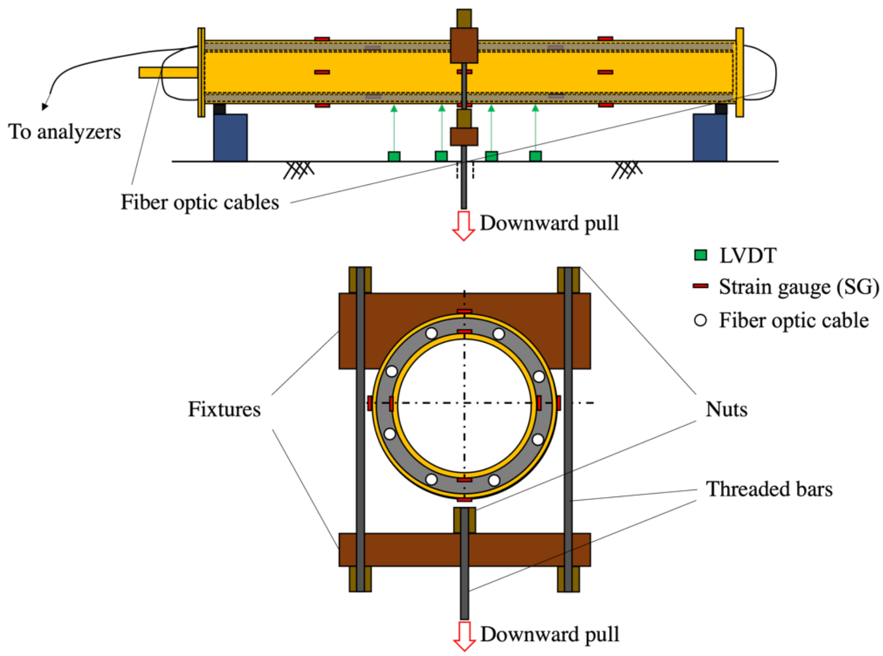

(b)

Figure 7 The mockup setup for the bending loading experiment: (a) an overview; (b) a schematic of cross-sections of the mockup.

The mockup was tested in three-point bending in three different directions as shown in Figure 8. The direction A was the initial configuration, whereas the direction B and C were subsequently set up by rotating the mockup 90 and 112.5 degrees clockwise from the initial configuration, respectively. The direction A is intended for the evaluation of the performance of Cable 2 against the LUNA measurement, whereas the direction B tests Cable 1 against the LUNA measurement. In the direction A, Cable 2 is positioned further away from the neutral plane ($y = 0$) (segment #3 and #7) than Cable 1 (segment #1 and #5), which provides Cable 2 with a greater sensitivity to capture bending deformation. Thus, the direction A is suited to the performance evaluation of Cable 2. The same logic applies to the direction B, which is optimized for the evaluation of Cable 1 performance. The direction C is intended for the direct comparison of the performance of Cable 1 and 2, as the distance from the neutral plane to the cable segments was identical for both cables in this loading configuration.

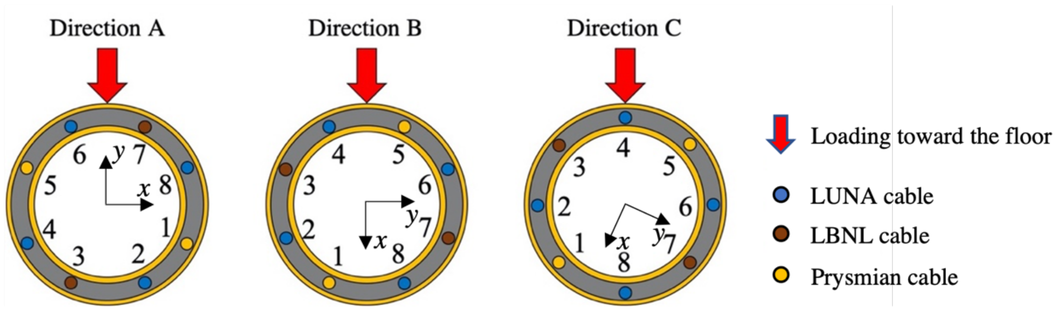

Figure 8 Loading directions with regard to the positions of the cable segments.

The loading was carried out sequentially in direction A, B, and C. Figure 9 shows the time series of bending loading in direction A. The load was increased by discrete increments in a stepwise manner. Each load increment was held for roughly ten to fifteen minutes so that fiber optic readings could be obtained from both Omnisens and LUNA interrogators. The Omnisens BOTDA performed a single measurement per load increment (~10 min), whereas the LUNA interrogator was taking ten readings per second (i.e., dynamic measurement at 10 Hz). Accumulated LUNA readings were averaged to produce one measurement per load increment to facilitate performance comparison with the Omnisens interrogator. It is noted that the room temperature did not change by more than $\pm 0.3^{o}$C during the entire testing period, which was measured by a handheld non-contact infrared thermometer. Hence, the effect of temperature change on fiber optic measurement results (Equation 1 and 2) is negligible.

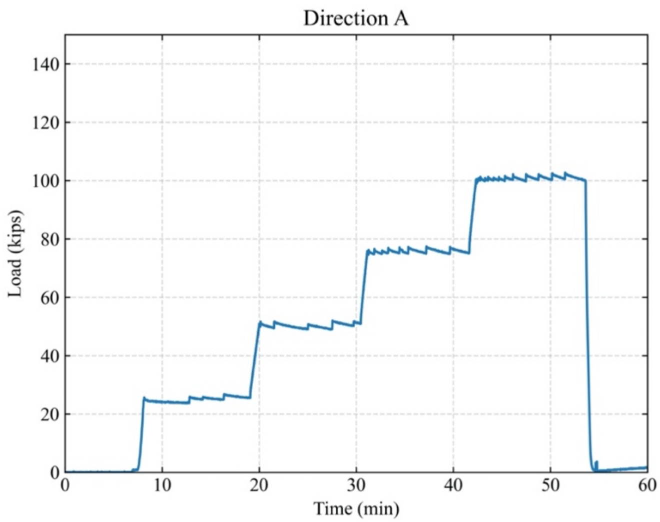

Figure 9 Loading time series for the direction A case.

Once the load level reached a specified limit, the mockup was unloaded and then rotated to change the loading direction. Another loading with stepwise increments was then resumed. The loading was kept in the elastic range of the mockup (< 100 kips (kilopounds) (1 kips = 4.448 kN)) for the direction A and B cases, whereas it was increased into the plastic range (> 100 kips) for the direction C case. Therefore, measurements in the direction A and B cases provided the cable performance for capturing elastic bending deformation of the well, while those in the direction C case provided that for measuring plastic bending deformation of the well.

4.2 BOTDA and OFDR measurement results

4.2.1 Direction A

Figure 10 shows strain changes along the mockup measured by the Omnisens BOTDA (Figure 10a) and the reference LUNA OFDR (Figure 10b) in the direction A case. Both figures show a triangular strain distribution at each load increment with the maximum (largest tension) and minimum (largest compression) strain magnitudes occurring at the middle of the mockup (i.e., 1.5 m) as expected in beam deformation in three-point bending.

The comparison between the BOTDA and LUNA results reveals that Cable 2 measured the peak tensile strain value of approximately 1,800 με, whereas LUNA measured 2,400 με, at the load level of 100 kips. It is noted that LUNA can measure local, submillimeter-scale strain profiles, whereas BOTDA measures averaged strain profiles over its spatial resolution (i.e., 0.75 m). By taking that into account, the difference in the maximum tensile strain levels measured by BOTDA (with Cable 2) and LUNA (with Cable 3) indicates good agreement between the two cables. The same is also true for the maximum compressive strain levels (i.e., segment 6 (Cable 3) vs. 7 (Cable 2)).

The above trends are also evident in the stress-strain curves at the center of the mockup (Figure 10c), as the BOTDA and LUNA stress-strain profiles are in good agreement with the latter consistently showing larger strain magnitudes at each stress level than the former. Note that the stress was calculated from the Bernoulli-Euler beam theory (i.e. $\sigma = (M/I)y$, where σ is the longitudinal stress, M is the bending moment, I is the second moment of area, and y is the distance from the neutral plane), so it represents an average theoretical bending stress in the composite steel-cement cross-section of the well mockup.

Due to the spatial averaging nature of the BOTDA measurement, the strain distributions in Figure 10a are smooth. In contrast, significant fluctuations are observed in the LUNA measurements on the tensile side (i.e., segment 2 and 4 in Figure 10b). As the fluctuations occur only on the tensile side, it is not solely due to the local nature of the LUNA measurement. The main cause is plastic deformation of the cement (where the fiber optic cables are embedded). The cement deformed plastically on the tensile side of the mockup creating miniature cracks (i.e., the upper half of the mockup cross section), whereas the compressive side (i.e., the lower half) remained largely intact as the tensile strength of cement is about one tenth of its compressive strength (Teodoriu et al. 2012).

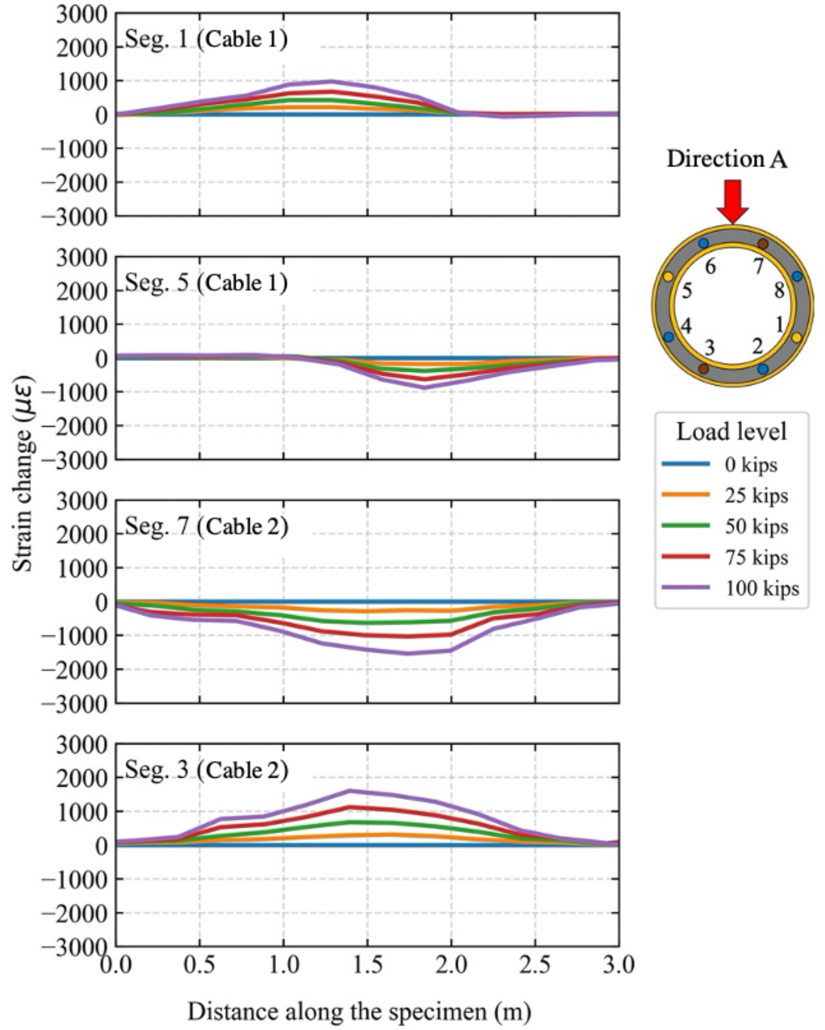

Seg. 1 (Cable 1)
Seg. 5 (Cable 1)
Seg. 7 (Cable 2)
Seg. 3 (Cable 2)
Strain change ($\mu\varepsilon$)
Distance along the specimen (m)
Direction A
6
7
5
8
4
1
3
2
Load level
0 kips
25 kips
50 kips
75 kips
100 kips

(a)

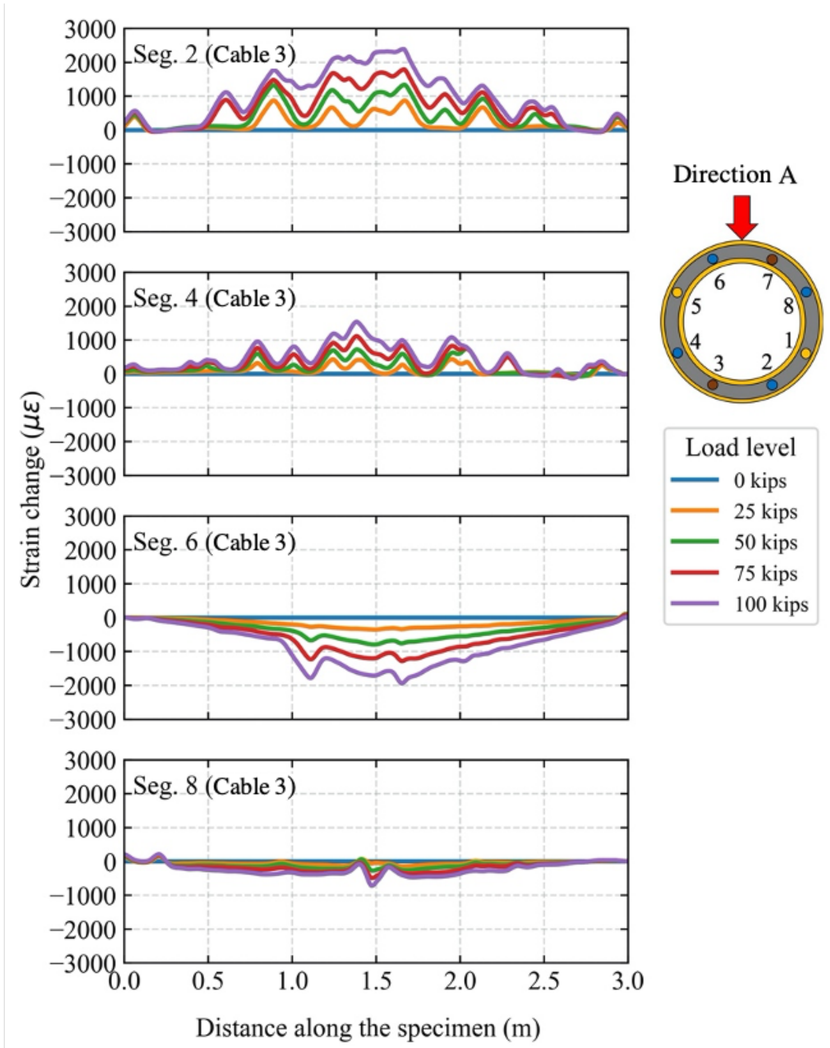

Seg. 2 (Cable 3)
Seg. 4 (Cable 3)
Seg. 6 (Cable 3)
Seg. 8 (Cable 3)
Strain change ($\mu\varepsilon$)
Distance along the specimen (m)
Direction A
1
2
3
4
5
6
7
8
Load level
0 kips
25 kips
50 kips
75 kips
100 kips

(b)

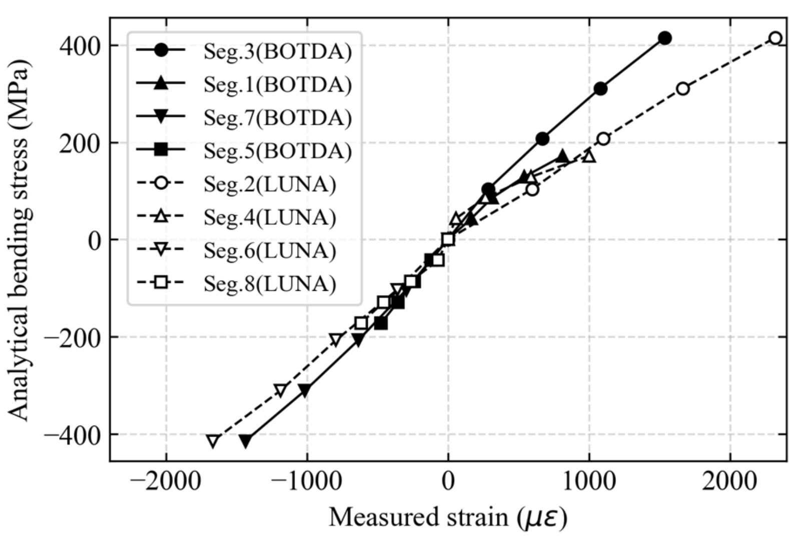

Seg.3(BOTDA)
Seg.1(BOTDA)
Seg.7(BOTDA)
Seg.5(BOTDA)
Seg.2(LUNA)
Seg.4(LUNA)
Seg.6(LUNA)
Seg.8(LUNA)
Analytical bending stress (MPa)
Measured strain ($\mu\varepsilon$)

(c)

Figure 10 Strain changes in the mockup during loading in the direction A: (a) Omnisens BOTDA readings along Cable 1 and 2; (b) reference LUNA OFDR readings along Cable 3; (c) analytical bending stress vs. measured strain at the center of the mockup.

4.2.2 Direction B

Figure 11 shows the strain development in the mockup during loading in the direction B case. It is observed that the maximum and minimum strain magnitudes at 100 kips for Cable 1 are approximately 1,800 $\mu\varepsilon$ and -1,300 $\mu\varepsilon$, respectively, whereas those for the reference Cable 3 are 2,700 $\mu\varepsilon$ and -1,700 $\mu\varepsilon$. The differences between Cable 1 and 3 results seem significant but if the strain values near the maximum and minimum values in the LUNA readings (Cable 3) are averaged over the spatial resolution of the Omnisens BOTDA (i.e., 0.75 m), these values decrease to approximately 2,000 $\mu\varepsilon$ and 1,500 $\mu\varepsilon$. Therefore, the LUNA readings are in good agreement with the values measured for Cable 1. That is, the strain sensing performance of Cable 1 is validated against the reference LUNA result.

Although it is not directly related to the cable performance, it is noteworthy that the tensile deformation in the cement during loading in the direction A case has been plastic (i.e., irreversible). This is suspected because strain fluctuations in the LUNA results are observed not only on the tensile side (i.e., segment 1, 2, 7, 8) but also on the compressive side at the segment 4, which was on the tensile side in the direction A case. Hence, the portions of the cement that were subjected to tensile deformation beforehand might no longer be elastic even though the mockup as a whole still behaved predominantly elastically against bending.

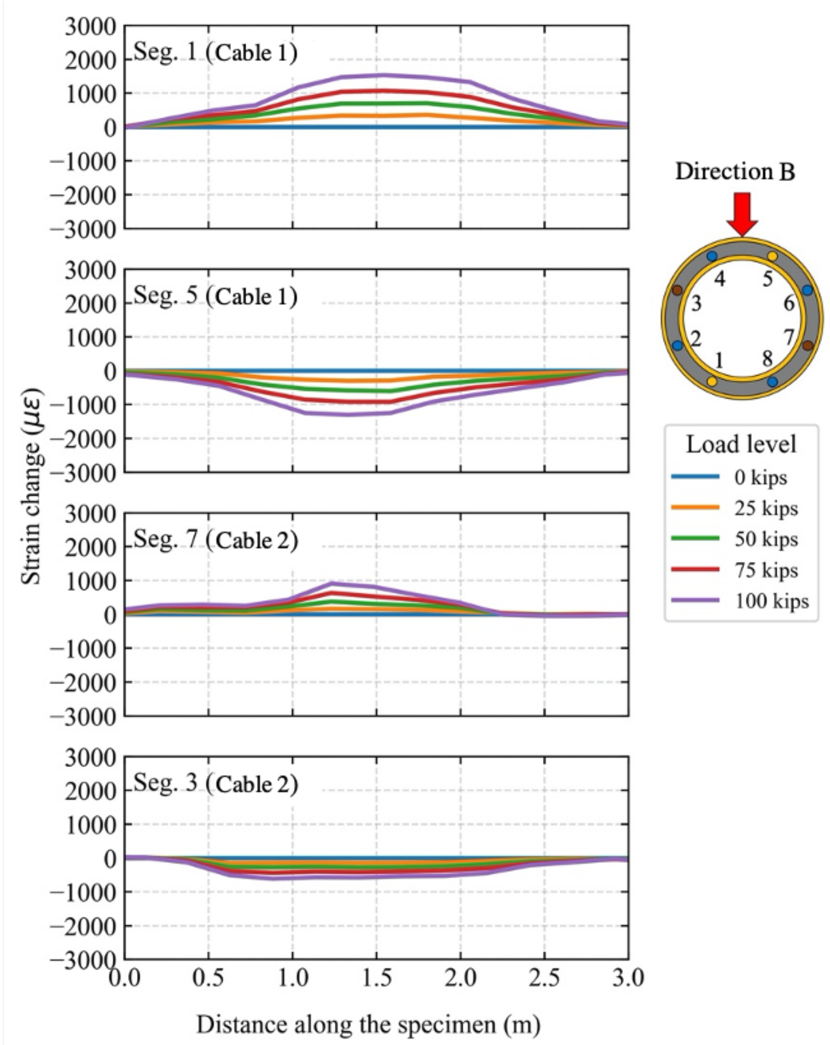

Seg. 1 (Cable 1)
Seg. 5 (Cable 1)
Seg. 7 (Cable 2)
Seg. 3 (Cable 2)
Strain change ($\mu\varepsilon$)
Distance along the specimen (m)
Direction B
Load level
0 kips
25 kips
50 kips
75 kips
100 kips

(a)

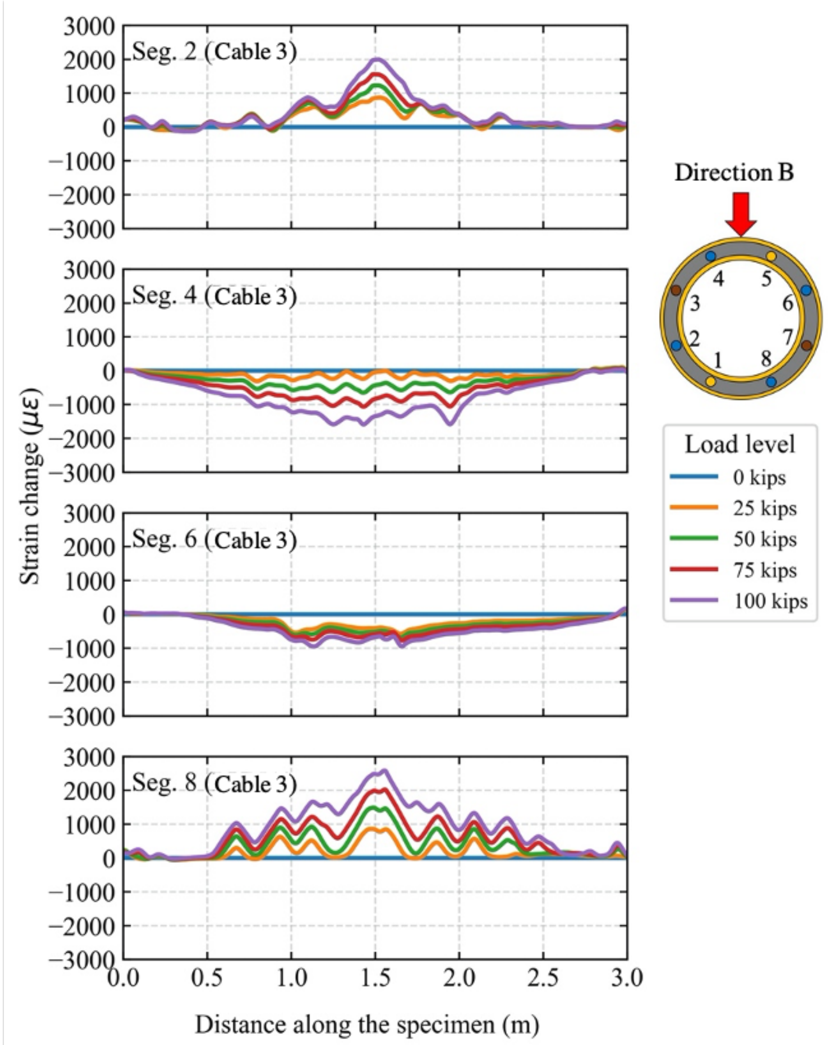

(b)

Figure 11 Strain changes in the mockup during loading in the direction B: (a) Omnisens BOTDA readings along Cable 1 and 2; (b) reference LUNA OFDR readings along Cable 3.

4.2.3 Direction C

Figure 12 shows the strain distributions during loading in the direction C case. Under direction A and B loading, the strain values for Cable 1 and 2 were noted to be comparable to those for the reference Cable 3, and hence the strain sensing performance of Cable 1 and 2 was validated. However, the strain sensing performance in the plastic range (i.e., loading in the direction C) varied significantly between the two cables. It is noted that the loading was terminated at 135 kips where the mockup accumulated bending deflection without an increase in bending load.

Figure 12a shows that the peak strain values at 135 kips for Cable 1 are larger than that for Cable 2. The maximum and minimum values are approximately 4,000 με and -3,000 με for Cable 1, whereas those are 3,000 με and -2,000 με for Cable 2. Also, the peak strain changes between 125 kips and 135 kips are much smaller for Cable 2 than for Cable 1. Of particular interest is the strain level decrease (instead of an increase) between 125 kips and 135kips for Cable 2 between 1.0 m and 1.5 m in the segment 7, which suggests slippage of the DSS fiber in Cable 2. Signs of DSS fiber slippage are not observed in Cable 1. The superior strain sensing performance of Cable 1 could be attributed to better attachment of its DSS FIMT to the surrounding polymer filling by means of pressure and/or adhesion. The DSS fiber in Cable 2 is not encased in a metal tube (instead it is covered in a second polymer coating), which might have hindered adhesion of the DSS fiber to the surrounding polymer layer that fills the space inside the metal tube.

The LUNA readings (Cable 3) cannot be compared directly with those the BOTDA readings for Cable 1 and 2 in the direction C case, as the distance from the neutral plane to Cable 3 was different than the distance to Cable 1 and 2. Larger strain magnitudes are expected for cables positioned further from the neutral plane (Cable 3 in segment 4 and 8) than those nearer to the neutral plane (Cable 1 and 2 in the segment 1, 3, 5, and 7). As expected, the peak strain magnitudes at 135 kips were significantly larger in Cable 3: approximately 7,000 με in segment 8 and -6,000 με in segment 4. If an average is taken over the spatial resolution of the Omnisens BOTDA (0.75 m), the peak values would decrease to roughly 5,000 με and -4,000 με, respectively. These values have to be multiplied by the ratio of distances from the neutral plane to facilitate a comparison with the peak values for Cable 1 and 2. The ratio is

$\sin 45^{\circ}/\sin 90^{\circ} = 0.71$. Therefore, the corrected strain values for Cable 3 would be roughly 3,600 με and -2,800 με, respectively. These values are in good agreement with those obtained in Cable 1 (4,000 με and -3,000 με), but slightly underestimated in Cable 2 (3,000 με and -2,000 με). This comparison reveals that Cable 1 demonstrates a better strain sensing performance than Cable 2 in the plastic bending deformation range of the mockup.

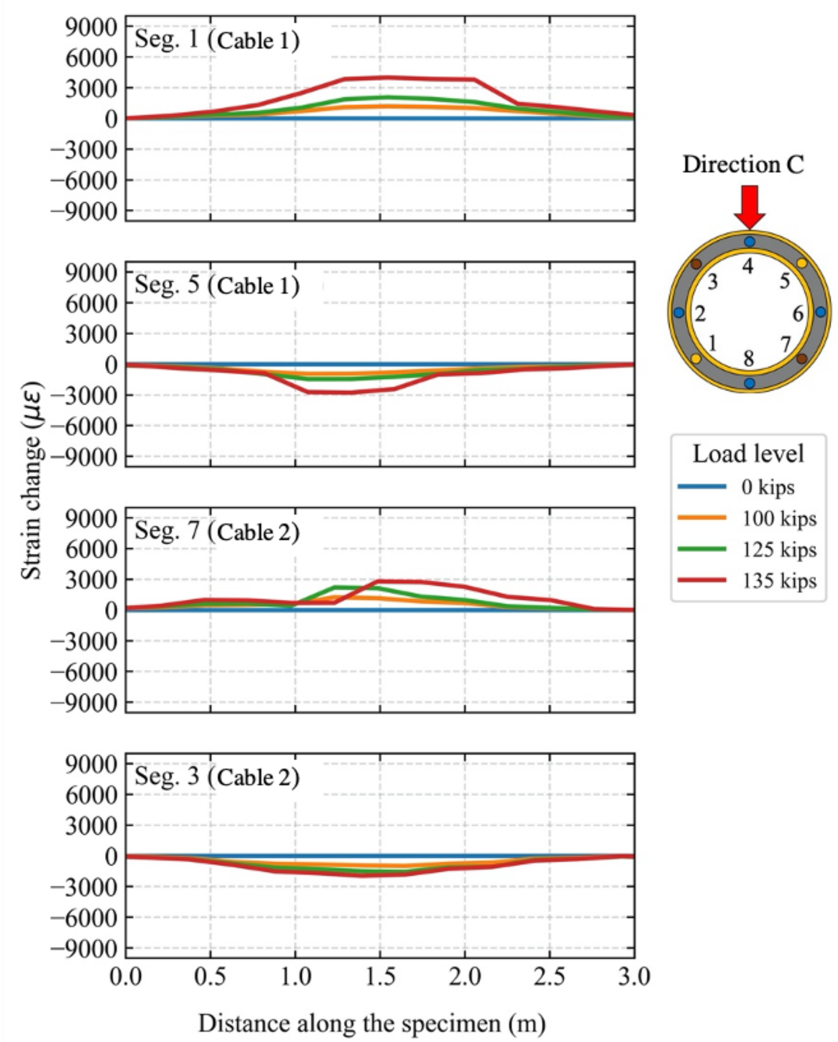

(a)

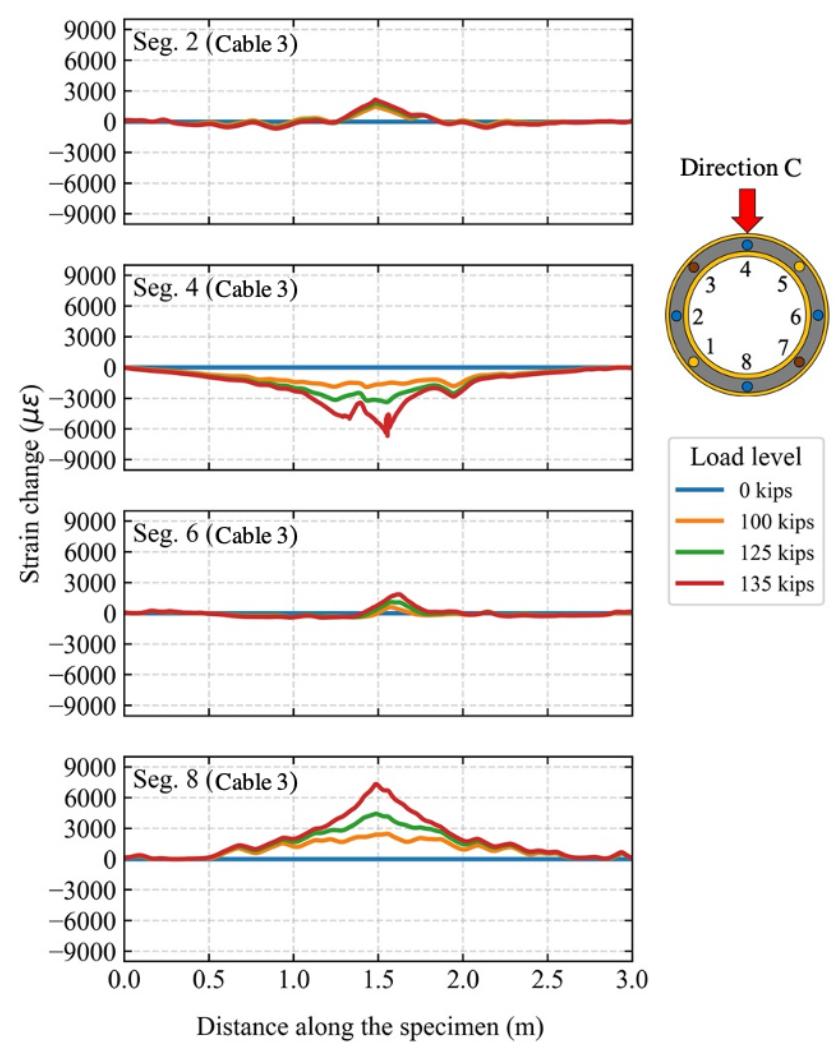

(b)

Figure 12 Strain changes in the mockup during loading in the direction C: (a) Omnisens BOTDA readings along Cable 1 and 2; (b) reference LUNA OFDR readings along Cable 3.

4.2.4 Temperature change

Although the evaluation of the strain sensing performance of fiber optic cables is the main focus of this study, the assessment of temperature sensing performance is also important, not only for DTS measurements with BOTDR/A but also for the temperature compensation of strain readings (Gue et al.

2015; Mohamad, Soga, and Amatya 2014; Pelecanos et al. 2018). Of particular importance is the isolation of temperature fibers from strains. BOTDR/A estimates temperature changes from the thermal expansion/contraction of DTS fibers, which are only several tens of microstrains per degree Celsius. Slight mechanical strains applied to the DTS fibers quickly distort the temperature measurement.

Strain isolation performance of the DTS fibers in Cable 1 and 2 are evaluated, in order to identify a key factor for achieving a better strain isolation of DTS fibers. Figure 13 shows temperature changes measured by the Omnisens BOTDA for Cable 1 and 2 during loading in the direction A case. The temperature changes are fictitious because the room temperature in the laboratory did not fluctuate by more than ±0.3˚C from 25˚C throughout the entire testing period, which was validated by infrared thermometer readings.

The erroneous temperature changes are caused by strain development in the DTS fibers in Cable 1 and 2. It is found that Cable 2 shows a significantly better strain isolation performance than Cable 1, as the magnitudes of the fictitious temperature changes are much smaller in Cable 2 than Cable 1 (e.g., roughly ±10˚C (Cable 1) vs. ±3˚C (Cable 2) at 100 kips) despite Cable 2 positioned further from the neutral plane.

The difference in the strain isolation performance of Cable 1 and 2 is attributed to the difference in the diameter of DTS FIMT: 1.8 mm OD for Cable 2 vs. 1.35 mm OD for Cable 1. The larger diameter DTS FIMT might have been able to accommodate strains without stretching/compressing the fibers encased in it. Also, the difference in stiffness of the belt material might have played a role (i.e., polyurethane (Cable 1) is softer than polypropylene (Cable 2)). It is noted that the DTS FIMTs in both Cable 1 and 2 were filled with gel so whether the FIMT was gel-filled or not is not a factor affecting the strain isolation performance herein. Also, the abovementioned trends of the fictitious temperature changes are found valid regardless of the loading direction (i.e., elastic or plastic loading range).

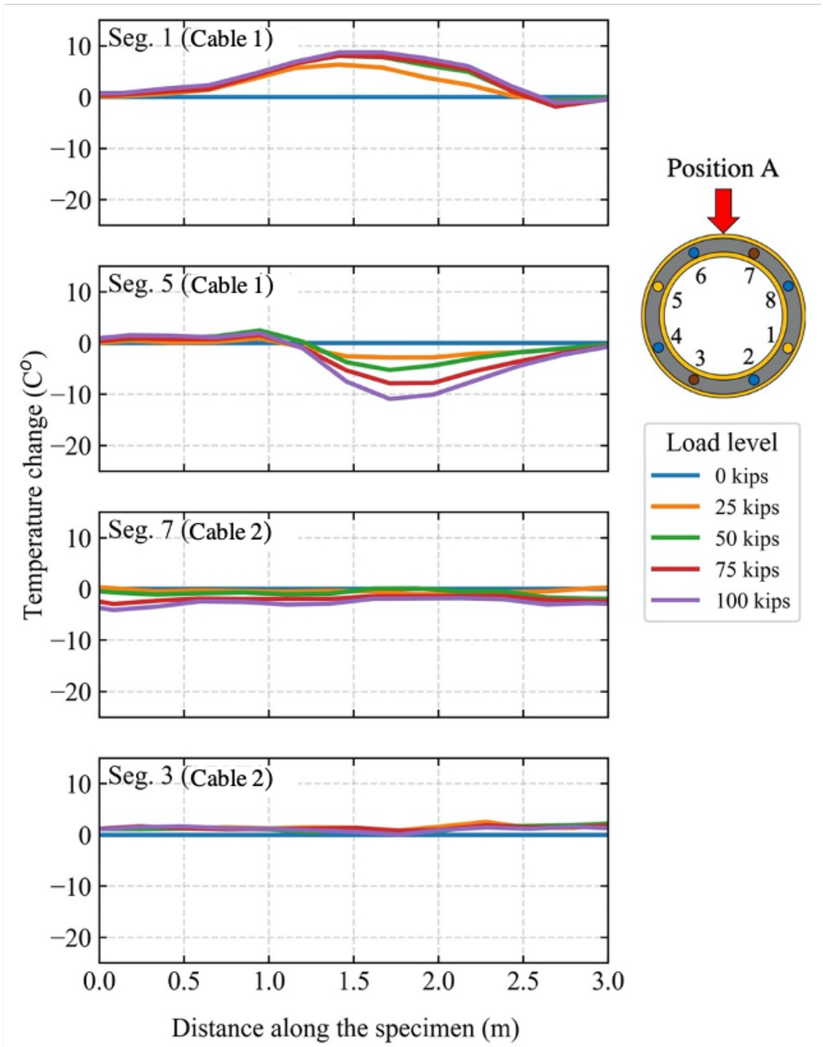

Figure 13 Fictitious temperature changes calculated from Omnisens BOTDA readings for Cable 1 and 2 during loading in the direction A.

5 Discussion

5.1 Bending curvature analysis

Curvature development of the mockup during loading is estimated from readings of the instrumented sensors. Bending curvature values from the strain gauges (SGs) and fiber optics are calculated from the following equation:

$$\kappa = (\epsilon_{lower} - \epsilon_{upper})/(2y) \tag{3}$$

where κ is the bending curvature, y is the distance from the neutral plane (see Figure 4); ϵ_{lower} is a strain value in the lower half of the mockup cross-section; ϵ_{upper} is a strain value in the upper half of the mockup cross-section. It is noted that ϵ_{lower} and ϵ_{upper} are chosen from a pair of strain gauges and fiber optic cables that are positioned diagonally across the mockup cross-section (e.g., segment 3 and 7, 1 and 5, 2 and 6, 4 and 8) at the same longitudinal distances. It is also noted that tension is taken as positive strain values.

An estimation of bending curvature from LVDT readings is carried out in the following manner. First, the flexural rigidity (*EI*) of the mockup under three-point bending is calculated from the following equation, which is transformed from the bending deflection formula for the Euler-Bernoulli beam:

$$EI = \begin{cases} (Pbx/6L\delta)(L^2 - b^2 - x^2) & if\ 0 \le x \le a \\ (Pa(L-x)/6L\delta)(L^2 - a^2 - (L-x)^2) & if\ a \le x \le L \end{cases} \tag{4}$$

where P is the vertical point load (obtained from load cell readings); L is the effective length of the mockup (= 2.92 m); δ is the deflection of the mockup (obtained from LVDT readings); x is the distance from the left-hand side boundary of the mockup, and a (= 1.44) and b (= 1.53) are the distances from the left- and right-hand side boundaries of the mockup to the point load, respectively. These parameters are schematically shown in Figure 14.

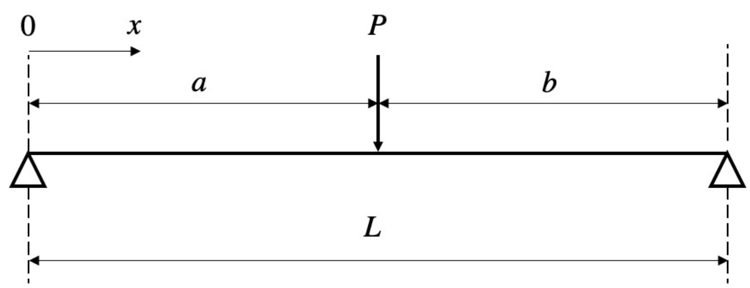

Figure 14 Beam model for three-point bending.

Second, bending moment is calculated from the following equation:

$$M = \begin{cases} P(1 - a/L)x & if\ 0 \leq x \leq a \\ Pa(x/L - 1) & if\ a \leq x \leq L \end{cases} \tag{5}$$

Finally, bending curvature is calculated from the following equation:

$$\kappa = M/EI \tag{6}$$

Results of the bending curvature estimation are provided in Figure 15 for the different loading directions. The curvature values are reported in m^{-1}, but the unit can be converted into radian/m and degrees/m by a factor of 1.0 and 57.296, respectively. The general trend is that the curvature distributions are triangular with a peak near the middle length of the mockup, which verifies the monitoring results against the theoretical curvature distributions under three-point bending. Also, the curvature values estimated by BOTDA are smaller than those by LUNA and other sensors, which is due to the spatial average nature of the BOTDR/A measurement with a longer gauge length (0.75 m).

Figure 15a shows that relative errors in peak curvature values (near the middle length of the mockup) between Cable 2 and the other sensors at 100 kips are roughly -45% (vs. LVDT), -8% (vs. SG), and -42% (vs. LUNA). Similarly, Figure 15b shows that relative errors for Cable 1, which are calculated to be roughly -36% (vs. LVDT), and -36% (vs. LUNA). This error comparison indicates that Cable 1 has a slightly better curvature monitoring performance than Cable 2, when the mockup deforms elastically in the direction A and B cases. Figure 15c shows a comparison of estimated bending curvature values for the direction C case when the mockup was subjected to plastic deformation. Relative errors in peak curvature values for Cable 2 at 135 kips are approximately -71% (vs. LVDT) and -104% (vs. LUNA), whereas those for Cable 1 are -24% (vs. LVDT) and -48% (vs. LUNA). This comparison reveals that the curvature monitoring performance of Cable 1 is better than that of Cable 2 in the plastic deformation range as well. It is noted that due to malfunction of some strain gauges, peak curvature values could not be obtained from strain gauge readings for the direction B and C cases.

In summary, Cable 1 provided better bending monitoring performance both in the examined elastic and plastic deformation ranges of the mockup. It should be noted, however, that the mockup deformation was still relatively small in the examined plastic range. Hence, curvature monitoring performance of Cable 1 and 2 at a greater plastic deformation range has to be examined carefully in a future study.

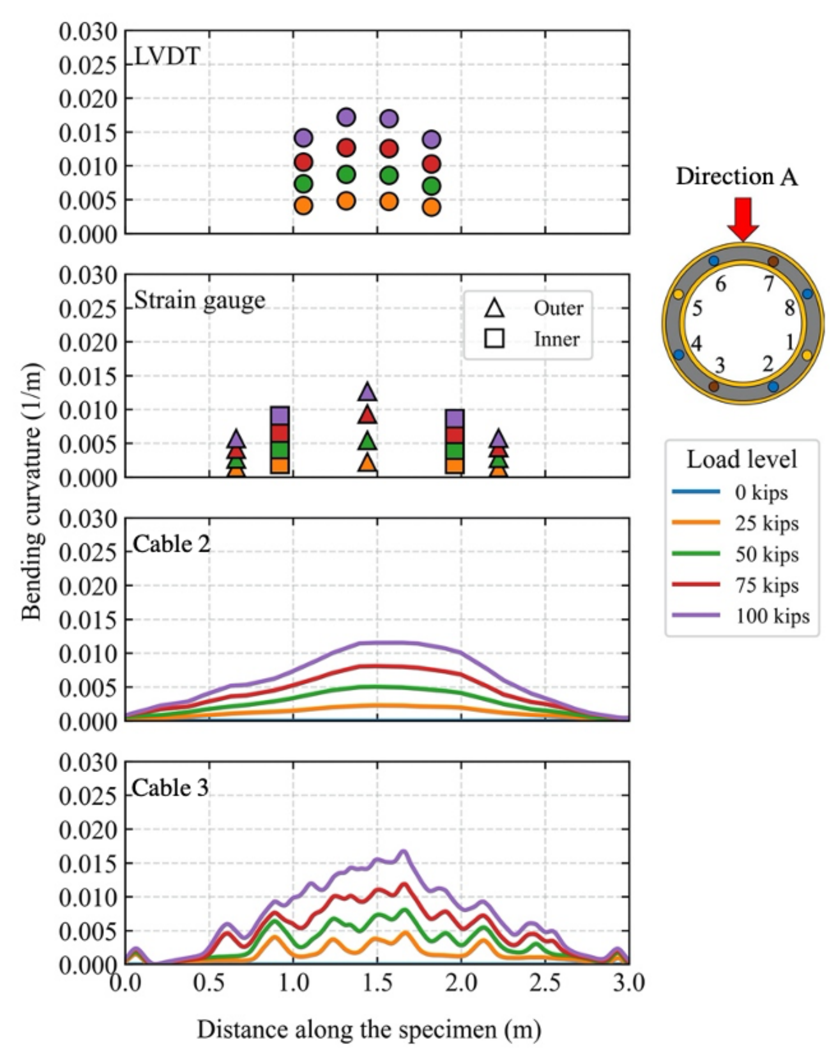
LVDT
Strain gauge
Outer
Inner
Cable 2
Cable 3
Bending curvature (1/m)
Distance along the specimen (m)
Direction A
Load level
0 kips
25 kips
50 kips
75 kips
100 kips

(a)

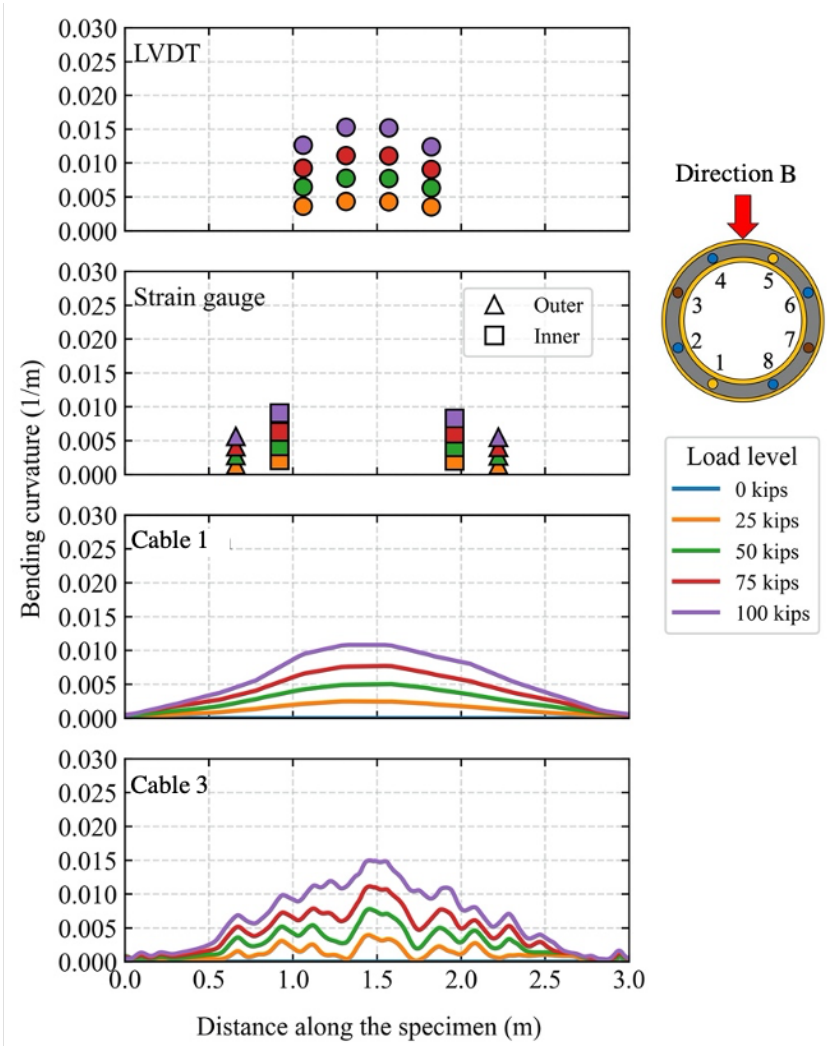
LVDT
Strain gauge
Outer
Inner
Cable 1
Cable 3
Bending curvature (1/m)
Distance along the specimen (m)
0.000
0.005
0.010
0.015
0.020
0.025
0.030
0.0
0.5
1.0
1.5
2.0
2.5
3.0
Direction B
1
2
3
4
5
6
7
8
Load level
0 kips
25 kips
50 kips
75 kips
100 kips

(b)

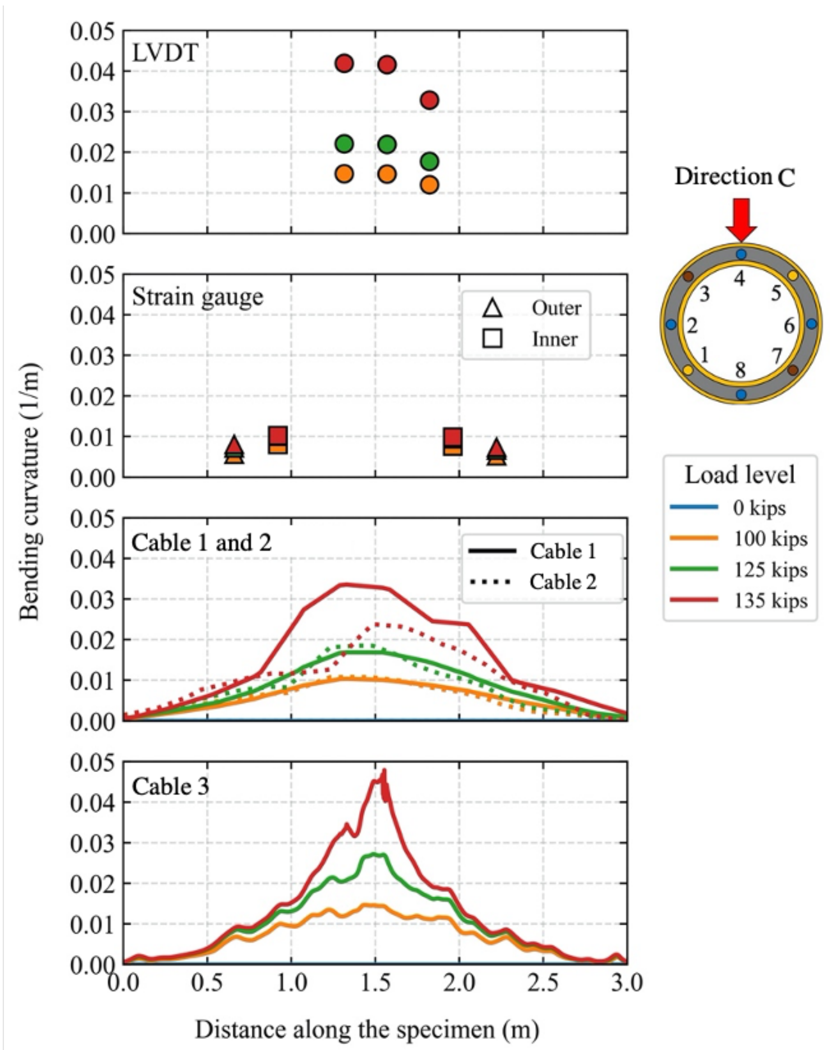

(c)

Figure 15 Bending curvature distributions of the mockup estimated from instrumented sensor readings: (a) Direction A; (b) Direction B; (c) Direction C.

5.2 Cable performance comparison

In order to carry out a performance comparison of the fiber optic cables examined in the present experiment, as well as those examined in a previous experiment, simple load vs. strain plots could not be utilized. This is because the bending stiffness of the well mockup in the present and previous experiments is found substantially different from each other; the mockup in the present test is softer than the one in the previous test. Although the steel pipes were made of the same material with the same dimensions in both experiments, and cement slurry was prepared from the identical ingredients with the identical procedure and cured in comparable conditions, small unknown differences during mockup preparation might have changed the bending stiffness of the mockups. Further review is required to identify the cause.

Consequently, bending curvature (fiber optics) vs. bending curvature (strain gauge and LVDT) plots are prepared for the performance comparison, which is presented in Figure 16. The reference curvature values are calculated from strain gauges and LVDT readings (horizontal axis), whereas curvature values from fiber optic measurements (vertical axis) at the corresponding locations (i.e., the same longitudinal locations as strain gauges and LVDTs) are obtained through linear interpolation of curvature distributions estimated from fiber optic readings.

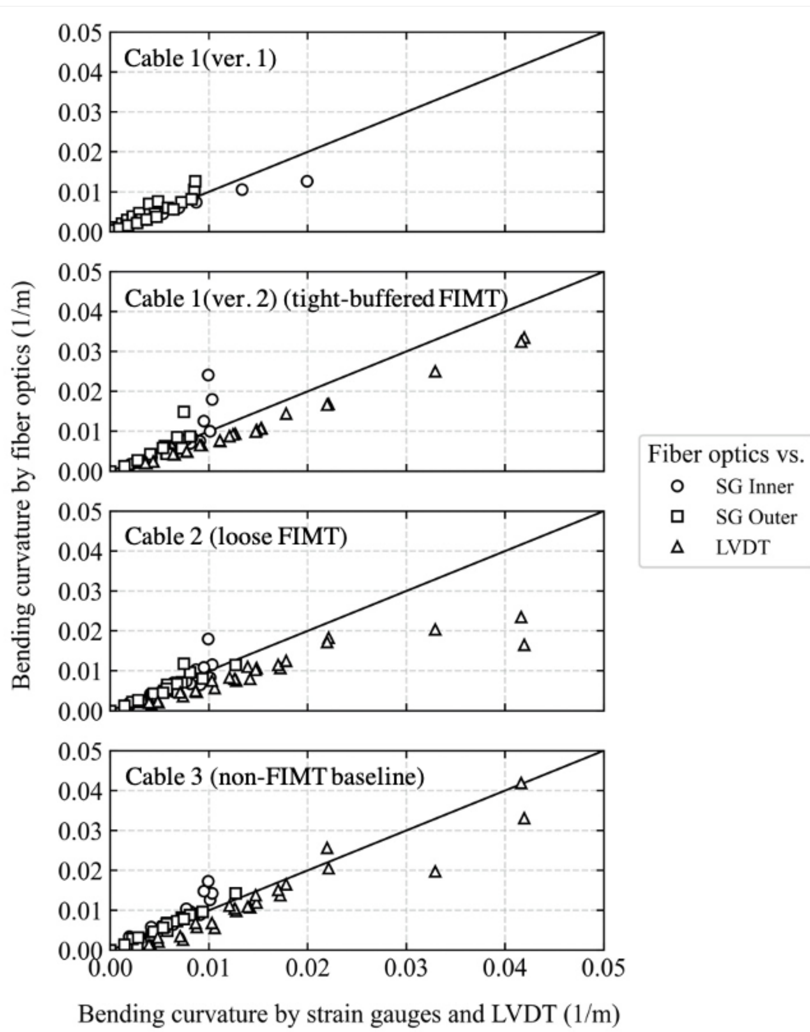

Figure 16 An evaluation of bending curvature monitoring performance of fiber optic cables against conventional sensors.

It is clear that the mockup was stiffer in the previous test, which manifested as the small curvature values for Cable 1 (version 1). It should be noted that the maximum load was 180 kips in the previous test vs. 135 kips in the present test. Although there are only a couple of data points in the plastic range ($\kappa \sim 0.01$ 1/m) for Cable 1 (version 1), its curvature monitoring performance is inferior to that of the other cables examined in the present experiment, as relative errors are -40% and -25% or less for Cable 1 (version 1) and the other cables at a reference curvature (*x*-axis) of 0.02 1/m, respectively.

The comparison between Cable 1 and 2 corroborates the performance evaluation discussed in earlier sections: Cable 1 is better suited for curvature monitoring than Cable 2 within the bending ranges examined in this study, as the data points for Cable 1 linearly align with the zero-error line, whereas those for Cable 2 are nonlinear at large curvature values ($\kappa > 0.02$ 1/m).

The deviation of the reference Cable 3 data points from the zero-error line for $0.03 < \kappa < 0.05$ 1/m is due to the spatial local nature of the LUNA measurement. The data points would align better if an averaging method is applied.

5.3 Comparison with existing research

It is argued that the results of this study are first-of-their-kind for several reasons. First, the cables used in this study are designed to have high robustness so that they will survive the harsh installation process of tubular in deep offshore wellbore. Existing studies on field applications of distributed strain sensing, in contrast, are limited to onshore wells whose construction processes were well-controlled to allow the use of fragile fiber optic cables (Zhang, Lei, Hashimoto, et al. 2020; Lei, Xue, and Hashimoto 2019; Zhang et al. 2019; Sun et al. 2020; Y. Zhang and Xue 2019; Sun et al. 2021; 2018). Second, the cables in this study were cemented in the annulus of the mockup without directly attaching them to the inner pipe (i.e., casing). This way of cable installation was performed because it mimics an actual installation process of tubular in an offshore well, which must be simple and efficient enough to comply with the stringent time constraint of the well construction process. In existing research, on the other hand, cables are usually attached directly on tubular by tapes and/or adhesives (Kogure and Okuda 2018; Earles et al. 2010; Pearce, Rambow, et al. 2009; Pearce, Legrand, et al. 2009), which is not feasible in actual field applications. Finally, the abovementioned research does not corroborate their fiber optic strain measurements with data from conventional sensors or analytical solutions. In other words, their fiber optic measurements are qualitative rather than quantitative. For these reasons, it is argued that the contribution of the present study on distributed strain sensing is unique, and it could lead to a step change in the use of distributed strain sensing for the environmental, management, and safety issues of natural gas production.

6 Conclusions

In this study, distributed strain sensing (DSS) of a well mockup subjected to three-point bending loading was carried out in the laboratory with BOTDR/A and OFDR fiber optic interrogators. The objective of this study was to examine the performance of custom-made fiber optic cables designed specifically for DSS monitoring of an oil and gas well. Key cable characteristics that affect their strain sensing performance were identified. In the experiment, a double pipe well mockup was constructed and fiber optic cables were instrumented in the mockup annulus which was then cemented. Strain gauges and LVDTs were also installed in the mockup to validate distributed fiber optic measurements.

The following findings are obtained from the analysis of experimental results:

(1) Tight-buffered optical fiber is necessary to achieve sufficient strain sensitivity in distributed strain sensing. Such a fiber optic cable can be manufactured by, for example, (i) encasing fiber in a metal tube (FIMT), (ii) applying the FIMT with a skim-coating polymer layer, and (iii) positioning the FIMT near the center of the cross-section of metal sheath (i.e., the outermost

sheath of the fiber optic cable) and filling the gap between the FIMT and metal sheath with polymer.

(2) It was demonstrated through laboratory testing that such a cable was capable of measuring both elastic and plastic bending deformations of the well mockup, whereas other cables, which lacked the abovementioned characteristics, failed to capture such deformations with accuracy.

(3) As to combined distributed strain and temperature sensing, it was found that the diameter of the gel-filled metal tube, where the optical fibers for the temperature measurement are embedded, would affect the accuracy of the temperature measurement, i.e., the diameter of the gel-filled tube needs to be large enough to isolate the temperature fibers from strains.

While this research focused on the performance of strain sensing cables in a well mockup under a simple bending load, further research is needed using well mockups under more complex loading and in a real subsurface environment. Future work may include, but not limited to the testing of the fabricated cable in a greater bending deformation range, testing under a combination of axial and bending loads, as well as the validation of the effect of the diameter of DTS FIMT on its strain isolation performance.

Acknowledgements

The authors are grateful for financial support provided by the MH21-S R&D consortium in the Ministry of Economy, Trade and Industry (METI) of the Japanese Government through Japan Oil, Gas and Metals National Corporation (JOGMEC). The authors are also appreciative of technical support provided by the manager and technicians of the 2nd-floor laboratory in Davis Hall (Shakhzod Takhirov, Matthew Cataleta, Llyr Griffith, and Phillip Wong) as well as graduate students and visiting researchers (Peter Hubbard, Hayato Nonaka, and Tianchen Xu) of the University of California, Berkeley. The authors would also like to thank those who are involved in the engineering and fabrication of the fiber optic cables examined in this research, namely, Phillip Morris, Dan Pacheco, and George Farrales from the Prysmian Group, and Karl Zimmermann and Mark Lowell from Lowell Innovation Consulting, LLC.

References

Aydin, G., 2014. Production Modeling in the Oil and Natural Gas Industry: An Application of Trend Analysis. Petroleum Science and Technology 32, 555–64. https://doi.org/10.1080/10916466.2013.825271.

———, 2015. Regression Models for Forecasting Global Oil Production. Petroleum Science and Technology 33, 1822–28. https://doi.org/10.1080/10916466.2015.1101474.

Aydin, G., Jang, H., Topal, E., 2016. Energy Consumption Modeling Using Artificial Neural Networks: The Case of the World's Highest Consumers. Energy Sources, Part B: Economics, Planning and Policy 11, 212–19. https://doi.org/10.1080/15567249.2015.1075086.

Butler, L.J., Gibbons, N., He, P., Middleton, C., Elshafie, M.Z.E.B., 2016. Evaluating the Early-Age Behaviour of Full-Scale Prestressed Concrete Beams Using Distributed and Discrete Fibre Optic Sensors. Construction and Building Materials 126, 894–912. https://doi.org/10.1016/j.conbuildmat.2016.09.086.

Chen, L., Feng, Y., Okajima, J., Komiya, A., Maruyama, S., 2018. Production Behavior and Numerical Analysis for 2017 Methane Hydrate Extraction Test of Shenhu, South China Sea. Journal of Natural Gas Science and Engineering 53, 55–66. https://doi.org/10.1016/j.jngse.2018.02.029.

Cola, S., Bersan, S., Michielin, E., Pangop, F.T., Simonini, P., Schenato, L., Palmieri, L., Bergamo, O., 2019. On Distributed Strains in a CFA Pile via DFOSs Measurements and Numerical Analysis. In Proceedings of the XVII ECSMGE-2019 https://www.issmge.org/uploads/publications/51/75/0717-

ECSMFE-2019_Cola.pdf.

Dale, B.A., Narahara, G.M., Stevens, R.M., 1996. A Case History of Reservoir Subsidence and Wellbore Damage Management in the South Belridge Diatomite Field. In Proceedings of the SPE Western Regional Meeting https://doi.org/10.2118/35658-ms.

Dou, H., Dong, X., Duan, Z., Ma, Y., Gao, D., 2020. Cement Integrity Loss Due to Interfacial Debonding and Radial Cracking during CO2 Injection. Energies 13, 1–17. https://doi.org/10.3390/en13174589.

Earles, D.M., Stoesz, C.W., Amaral, A.S., Pearce, J.G., Dejongh, H.A., Rambow, F.H.K., 2010. Real-Time Monitoring of Sand Control Completions. In Proceedings of the SPE Annual Technical Conference and Exhibition https://doi.org/10.2118/134555-ms.

Fabris, C., Schweiger, H.F., Pulko, B., Woschitz, H., Račanský, V., 2021. Numerical Simulation of a Ground Anchor Pullout Test Monitored with Fiber Optic Sensors. Journal of Geotechnical and Geoenvironmental Engineering 147, 04020163. https://doi.org/10.1061/(asce)gt.1943-5606.0002442.

Fredrich, J.T., Arguello, J.G., Deitrick, G.L., Rouffignac, E.P., 2000. Geomechanical Modeling of Reservoir Compaction, Surface Subsidence, and Casing Damage at the Belridge Diatomite Field. SPE Reservoir Evaluation & Engineering 3, 8–10. https://doi.org/10.2118/65354-PA.

Gasda, S.E., Bachu, S., Celia, M.A., 2004. Spatial Characterization of the Location of Potentially Leaky Wells Penetrating a Deep Saline Aquifer in a Mature Sedimentary Basin. Environmental Geology 46, 707–20. https://doi.org/10.1007/s00254-004-1073-5.

Gue, C. Y., Wilcock, M., Alhaddad, M. M., Elshafie, M. Z. E. B., Soga, K., Mair, R. J., 2015. The Monitoring of an Existing Cast Iron Tunnel with Distributed Fibre Optic Sensing (DFOS). Journal of Civil Structural Health Monitoring 5, 573–86. https://doi.org/10.1007/s13349-015-0109-8.

Hickman, S.H., Hsieh, P.A., Mooney, W.D., Enomoto, C.B., Nelson, P.H., Mayer, L.A., Weber, T.C., Moran, K., Flemings, P.B., McNutt, M.K., 2012. Scientific Basis for Safely Shutting in the Macondo Well after the April 20, 2010 Deepwater Horizon Blowout. Proceedings of the National Academy of Sciences of the United States of America 109, 20268–73.

https://doi.org/10.1073/pnas.1115847109.
Inaudi, D., Glisic, B., 2006. Fiber Optic Sensing for Innovative Oil and Gas Production and Transport Systems. Optical Fiber Sensors , 4. https://doi.org/10.1364/OFS.2006.FB3.
Kechavarzi, C., Soga, K., Battista, N. de, Pelecanos, L., Elshafie, M.Z.E.B., Mair, R.J., 2016. *Distributed Optical Fibre Sensing for Monitoring Civil Infrastructure - A Practical Guide*. https://www.icevirtuallibrary.com/isbn/9780727760555.
Klar, A., Bennett, P.J., Soga, K., Mair, R.J., Tester, P., Fernie, R., St John, H.D., Torp-Peterson, G., 2006. Distributed Strain Measurement for Pile Foundations. Proceedings of the Institution of Civil Engineers - Geotechnical Engineering 159, 135–44. https://doi.org/10.1680/geng.2006.159.3.135.
Klar, A., Deerberg, G., Janicki, G., Schicks, J., Riedel, M., Fietzek, P., Mosch, T., et al., 2019. Marine Gas Hydrate Technology : State of the Art and Future Possibilities for Europe. Marine Gas Hydrate – an Indigenous Resource of Natural Gas for Europe (MIGRATE) https://doi.org/10.3289/MIGRATE_WG2.2019.
Kogure, T., Okuda, Y., 2018. Monitoring the Vertical Distribution of Rainfall-Induced Strain Changes in a Landslide Measured by Distributed Fiber Optic Sensing With Rayleigh Backscattering. Geophysical Research Letters 45, 4033–40. https://doi.org/10.1029/2018GL077607.
Krietsch, H., Gischig, V., Jalali, M.R., Doetsch, J., Valley, B., Amann, F., 2018. A Comparison of FBG- and Brillouin-Strain Sensing in the Framework of a Decameter-Scale Hydraulic Stimulation Experiment Conference. In Proceedings of the 52nd US Rock Mechanics / Geomechanics Symposium https://onepetro.org/ARMAUSRMS/proceedings-abstract/ARMA18/All-ARMA18/ARMA-2018-800/122534.
Lei, X., Xue, Z., Hashimoto, T., 2019. Fiber Optic Sensing for Geomechanical Monitoring: (2)- Distributed Strain Measurements at a Pumping Test and Geomechanical Modeling of Deformation of Reservoir Rocks. Applied Sciences 9, 417. https://doi.org/10.3390/app9030417.
Mayuga, M.N., Allen, D.R., 1969. Subsidence in the Wilmington Oil Field, Long Beach, California,

U.S.A. In Proceedings of the Tokyo Symposium on Land Subsidence, International Association of Scientific Hydrology, Studies and Reports in Hydrology, IASH-UNESCO 1, http://www.saveballona.org/gasoilfields/WilmSubGC.pdf.

McNutt, M.K., Camilli, R., Crone, T.J., Guthrie, G.D., Hsieh, P.A., Ryerson, T.B., Savas, O., Shaffer, F., 2012. Review of Flow Rate Estimates of the Deepwater Horizon Oil Spill. Proceedings of the National Academy of Sciences of the United States of America 109, 20260–67. https://doi.org/10.1073/pnas.1112139108.

McNutt, M.K., Chu, S., Lubchenco, J., Hunter, T., Dreyfus, G., Murawski, S.A., Kennedy, D.M., 2012. Applications of Science and Engineering to Quantify and Control the Deepwater Horizon Oil Spill. Proceedings of the National Academy of Sciences of the United States of America 109, 20222–28. https://doi.org/10.1073/pnas.1214389109.

Mohamad, H., Bennet, P.J., Soga, K., Mair, R.J., Bowers, K., 2010. Behaviour of an Old Masonry Tunnel Due to Tunnelling Induced Ground Settlement. Géotechnique 60, 927–38. https://doi.org/10.1680/geot.8.p.074.

Mohamad, H., Soga, K., Amatya, B., 2014. Thermal Strain Sensing of Concrete Piles Using Brillouin Optical Time Domain Reflectometry. Geotechnical Testing Journal 37, https://doi.org/10.1520/GTJ20120176.

Mohamad, H., Soga, K., Bennett, P.J., Mair, R.J., Lim, C.S., 2012. Monitoring Twin Tunnel Interactions Using Distributed Optical Fiber Strain Measurements. Journal of Geotechnical and Geoenvironmental Engineering, ASCE 138, 957–67. https://doi.org/10.1061/(ASCE)GT.1943-5606.0000656.

Mohamad, H., Soga, K., Pellew, A., Bennett, P.J., 2011. Performance Monitoring of a Secant-Piled Wall Using Distributed Fiber Optic Strain Sensing. Journal of Geotechnical and Geoenvironmental Engineering 137, 1236–43. https://doi.org/10.1061/(asce)gt.1943-5606.0000543.

Nagel, N. B., 2001. Compaction and Subsidence Issues within the Petroleum Industry: From Wilmington to Ekofisk and Beyond. Physics and Chemistry of the Earth, Part A: Solid Earth and Geodesy 26, 3–

14. https://doi.org/10.1016/S1464-1895(01)00015-1.

Pearce, J.G., Legrand, P., Dominique, T., Childers, B. A., Rambow, F.H.K., Dria, D. E., 2009. Real-Time Compaction Monitoring with Fiber-Optic Distributed Strain Sensing (DSS). In Proceedings of the SPWLA 50th Annual Logging Symposium https://www.onepetro.org/conference-paper/SPWLA-2009-85310.

Pearce, J.G., Rambow, F.H.K., Shroyer, W., Huckabee, P., Jongh, H. de, Dria, D. E., Childers, B. A., Hall, T. S., Dominique, T., 2009. High Resolution, Real-Time Casing Strain Imaging for Reservoir and Well Integrity Monitoring: Demonstration of Monitoring Capability in a Field Installation. In Proceedings of the 2009 SPE Annual Technical Conference and Exhibition https://doi.org/10.2118/124932-ms.

Pelecanos, L., Soga, K., Chunge, M.P.M., Ouyang, Y., Kwan, V., 2017. Distributed Fibre-Optic Monitoring of an Osterberg-Cell Pile Test in London. Géotechnique Letters 7, 1–9. https://doi.org/10.1680/jgele.16.00081.

Pelecanos, L., Soga, K., Elshafie, M.Z. E. B., Battista, N. de, Kechavarzi, C., Gue, C. Y., Ouyang, Y., Seo, H.-J., 2018. Distributed Fiber Optic Sensing of Axially Loaded Bored Piles. Journal of Geotechnical and Geoenvironmental Engineering 144, 1–16. https://doi.org/10.1061/(ASCE)GT.1943-5606.0001843.

Rabaiotti, C., Hauswirth, D., Fischli, F., Facchini, M., Puzrin, A., 2017. Structural Health Monitoring of Airfield Pavements Using Distributed Fiber-Optics Sensing. In Proceedings of the 4th Conf. on Smart Monitoring, Assessment and Rehabilitation of Civil Structures (SMAR 2017) https://data.smar-conferences.org/SMAR_2017_Proceedings/papers/133.pdf.

Roberts, D, 1953. Shear Prevention in the Wilmington Field. https://www.onepetro.org/conference-paper/API-53-146.

Sasaki, T., 2019. Fibre Optic Monitoring and Finite Element Analysis of Well Integrity in Methane Hydrate Reservoirs. https://doi.org/10.17863/CAM.41244.

Sasaki, T., Park, J., Soga, K., Momoki, T., Kawaguchi, K., Muramatsu, H., Imasato, Y., Balagopal, A., Fontenot, J., Hall, T., 2019. Distributed Fibre Optic Strain Sensing of an Axially Deformed Well Model in the Laboratory. Journal of Natural Gas Science and Engineering https://doi.org/10.1016/j.jngse.2019.103028.

Schwall, G. M, Denney, C. A, 1994. Subsidence Induced Casing Deformation Mechanisms in the Ekofisk Field. In Proceedings of the 1994 Eurock SPE/ISRM Rock Mechanics in Petroleum Engineering Conference https://doi.org/10.2118/28091-MS.

Soga, K., Luo, L., 2018. Distributed Fiber Optics Sensors for Civil Engineering Infrastructure Sensing. Journal of Structural Integrity and Maintenance 3, 1–21. https://doi.org/10.1080/24705314.2018.1426138.

Sun, Y., Xue, Z., Hashimoto, T., Lei, X., Zhang, Y., 2020. Distributed Fiber Optic Sensing System for Well-Based Monitoring Water Injection Tests—A Geomechanical Responses Perspective. Water Resources Research 56, https://doi.org/10.1029/2019WR024794.

Sun, Y., Xue, Z., Hashimoto, T., Zhang, Y., 2021. Optically Quantifying Spatiotemporal Responses of Water Injection-Induced Strain via Downhole Distributed Fiber Optics Sensing. Fuel 283, 118948. https://doi.org/10.1016/j.fuel.2020.118948.

Sun, Y., Xue, Z., Zhang, Y., Hashimoto, T., Park, H., 2018. Field Measurements Using Distributed Fiber-Optic Sensing Technology and Numerical Simulation of Geomechanical Deformation Caused by CO2 Injection. In Proceedings of the 14th International Conference on Greenhouse Gas Control Technologies, GHGT-14 https://papers.ssrn.com/sol3/papers.cfm?abstract_id=3365651.

Teodoriu, C., Yuan, Z., Schubert, J., Amani, M., 2012. Experimental Measurements of Mechanical Parameters of Class G Cement. In Proceedings of the SPE/EAGE European Unconventional Resources Conference and Exhibition https://doi.org/10.2118/153007-MS.

Wu, Q., 2019. Advanced Distributed Fiber Optic Sensors for Monitoring Real-Time Cementing Operations and Long Term Zonal Isolation. https://repositories.lib.utexas.edu/handle/2152/77392.

Yamamoto, K., 2015. Overview and Introduction: Pressure Core-Sampling and Analyses in the 2012-

2013 MH21 Offshore Test of Gas Production from Methane Hydrates in the Eastern Nankai Trough. Marine and Petroleum Geology 66, 296–309. https://doi.org/10.1016/j.marpetgeo.2015.02.024.

Yamamoto, K., Dallimore, S.R., 2008. Aurora-JOGMEC-NRCan Mallik 2006-2008 Gas Hydrate Research Project Progress. Fire in the Ice Summer, 1–5. https://netl.doe.gov/sites/default/files/publication/HMNewsSummer08.pdf.

Yamamoto, K., Kanno, T., Wang, X.-X., Tamaki, M., Fujii, T., Chee, S.-S., Wang, X.-W., Pimenov, V., Shako, V., 2017. Thermal Responses of a Gas Hydrate-Bearing Sediment to a Depressurization Operation. RSC Advances 7, 5554–77. https://doi.org/10.1039/C6RA26487E.

Yamamoto, K., Terao, Y., Fujii, T., Ikawa, T., Seki, M., Matsuzawa, M., Kanno, T., 2014. Operational Overview of the First Offshore Production Test of Methane Hydrates in the Eastern Nankai Trough. In Proceedings of the Offshore Technology Conference https://doi.org/10.4043/25243-MS.

Yoneda, J., Masui, A., Konno, Y., Jin, Y., Egawa, K., Kida, M., Ito, T., Nagao, J., Tenma, N., 2015. Mechanical Properties of Hydrate-Bearing Turbidite Reservoir in the First Gas Production Test Site of the Eastern Nankai Trough. Marine and Petroleum Geology 66, 471–86. https://doi.org/10.1016/j.marpetgeo.2015.02.029.

Yudovich, A., Chin, L.V., Morgan, D.R., 1988. Casing Deformation in Ekofisk. In Proceedings of the Offshore Technology Conference https://doi.org/10.4043/5623-ms.

Zhang, C.C., Shi, B., Gu, K., Liu, S.P., Wu, J.H., Zhang, S., Zhang, L., Jiang, H.T., Wei, G.Q., 2018. Vertically Distributed Sensing of Deformation Using Fiber Optic Sensing. Geophysical Research Letters 45, 11,732-11,741. https://doi.org/10.1029/2018GL080428.

Zhang, S., Liu, H., Cheng, J., DeJong, M.J., 2020. A Mechanical Model to Interpret Distributed Fiber Optic Strain Measurement at Displacement Discontinuities. Structural Health Monitoring https://doi.org/10.1177/1475921720964183.

Zhang, S., Liu, H., Coulibaly, A.A.S., DeJong, M.J., 2020. Fiber Optic Sensing of Concrete Cracking and Rebar Deformation Using Several Types of Cable. Structural Control and Health Monitoring 1–23. https://doi.org/10.1002/stc.2664.

Zhang, Y., Lei, X., Hashimoto, T., Xue, Z., 2020. In Situ Hydromechanical Responses during Well Drilling Recorded by Fiber-Optic Distributed Strain Sensing. Solid Earth 11, 2487–97. https://doi.org/10.5194/se-11-2487-2020.

Zhang, Y., Xue, Z., 2019. Deformation-Based Monitoring of Water Migration in Rocks Using Distributed Fiber Optic Strain Sensing: A Laboratory Study. Water Resources Research 55, 8368–83. https://doi.org/10.1029/2019WR024795.

Zhang, Y., Xue, Z., Park, H., Shi, J.-Q., Kiyama, T., Lei, X., Sun, Y., Liang, Y., 2019. Tracking CO2 Plumes in Clay-Rich Rock by Distributed Fiber Optic Strain Sensing (DFOSS): A Laboratory Demonstration. Water Resources Research 55, 856–67. https://doi.org/10.1029/2018WR023415.